

CrystEngComm

Accepted Manuscript



This is an *Accepted Manuscript*, which has been through the Royal Society of Chemistry peer review process and has been accepted for publication.

Accepted Manuscripts are published online shortly after acceptance, before technical editing, formatting and proof reading. Using this free service, authors can make their results available to the community, in citable form, before we publish the edited article. We will replace this *Accepted Manuscript* with the edited and formatted *Advance Article* as soon as it is available.

You can find more information about *Accepted Manuscripts* in the [Information for Authors](#).

Please note that technical editing may introduce minor changes to the text and/or graphics, which may alter content. The journal's standard [Terms & Conditions](#) and the [Ethical guidelines](#) still apply. In no event shall the Royal Society of Chemistry be held responsible for any errors or omissions in this *Accepted Manuscript* or any consequences arising from the use of any information it contains.

Synthesis and thermometric property of shuttle-like $\text{Er}^{3+}/\text{Yb}^{3+}$ co-doped $\text{NaLa}(\text{MoO}_4)_2$ microstructures

Dong He^a, Chongfeng Guo^{a*}, Shaoshuai Zhou^b, Liangliang Zhang^c, Zheng Yang^a, Changkui Duan^b, Min Yin^b

a. National Key Laboratory of Photoelectric Technology and Functional Materials (Culture Base) in Shaanxi Province, National Photoelectric Technology and Functional Materials & Application of Science and Technology International Cooperation Base, Institute of Photonics & Photon-Technology, Northwest University, Xi'an, 710069, China;

b. School of Physical Science, University of Science and Technology of China, Hefei, 230026, China;

c. State key Laboratory for Manufacturing Systems Engineering, Xi'an Jiaotong University, Xi'an 710049, China.

* Author to whom correspondence should be addressed

Tel. & Fax.: 86-29-88302661

E-mail: guocf@nwu.edu.cn (Prof. Guo)

Abstract

$\text{Yb}^{3+}/\text{Er}^{3+}$ co-doped $\text{NaLa}(\text{MoO}_4)_2$ up-conversion (UC) mono-disperse shuttle-like microcrystals were prepared by hydrothermal method without any organic *solvents* or surfactants. The phase purity, structure and morphologies of the samples were characterized by X-ray diffraction (XRD), field emission scanning electron microscope (FE-SEM) and transmission electron microscope (TEM). The effects of the initial reaction solution pH values and reaction time on the morphologies of final products were investigated. Temperature-dependent UC luminescence and temperature sensing properties of samples were discussed according to the fluorescence intensity ratio (FIR) of green emissions from ${}^2\text{H}_{11/2}/{}^4\text{S}_{3/2} \rightarrow {}^4\text{I}_{15/2}$ transitions of Er^{3+} at 530 and 550 nm in the range of 300-510 K with excitation of 980 nm laser. After sintering at 600 °C for 1 h, the UC intensity of sample is raised about 1070 times than that of sample without calcinations, and the maximum sensitivity of the samples with and without *calcinations* is approximately 0.0131 K^{-1} at 510 K and 0.0135 K^{-1} at 450 K, respectively. Results indicate that the sensitivity is hardly dependent on UC luminescence *intensities* of samples, and the present shuttle-like $\text{NaLa}(\text{MoO}_4)_2$ mono-dispersed *micro-crystals* exhibited excellent temperature sensing properties.

Keywords: Up-conversion; Thermometry; Hydrothermal; Micro-crystals.

Introduction

Photon up-conversion (UC) through rare earth (RE) doped luminescent materials *have* aroused great interest due to *their abilities* to generate photons at shorter wavelengths than the excitation wavelength after laser stimulation, which *exhibit* useful applications in three-dimensional displays, solar cells, fiber amplifiers, thermometry and anti-counterfeit markers [1]. As a unique class of optical materials, UC *phosphor shows* a possibility of excitation by near infrared (NIR), such as 980 or 808 nm laser, which can penetrate biological media and no auto-fluorescence, therefore they are ideal luminescent materials for bio-imaging labels, biological sensing and photo-activated therapeutic agent [2-4]. Especially, the widespread research in the field of UC micro-/nano-materials motivates their applications in biology. Temperature is the most fundamental parameter in biology, such as metabolism, enzyme reaction and precancerous lesion are marked by temperature change, thus accurate determination of intracellular temperature is very important for the disease diagnose and therapy [5, 6]. Conventional contact thermometer that based on the principle of metal *or* liquid expansion is not suitable for the application in biological fields due to its larger size [7]. It is an urgent task to develop micro- and nano-*scaled* small size (the size < 10 μm) thermometer with high resolution [8]. Much effort has made to design small size optical temperature sensor [9-11], the optical thermometry based on *fluorescence intensity ratio (FIR) technique using temperature-dependent UC luminescence (UCL)* intensities from two thermally coupled energy levels (TCLs) of RE ions *has* attracted more attention [12-14]. Here, the relative population of two thermally coupled levels *follows Boltzmann-type* population distribution, which implies that their energy level difference (ΔE) can not be too big or too small (generally range from 200 to 2000 cm^{-1}) [15]. Among the RE ions, Er^{3+} - Yb^{3+} co-doped UC phosphors have been extensively investigated as potential optical temperature sensor because two suitable TCLs ($^2\text{H}_{11/2}$ and $^4\text{S}_{3/2}$) of Er^{3+} and intense broad absorption (ranging from 850-1050 nm) of Yb^{3+} [16]. More importantly, the effectively energy transfer from Yb^{3+} to Er^{3+} under commercialized 980 nm near infrared (NIR) laser diode *has* been proved to easily occur [17]. Meanwhile, UC inorganic luminescent materials have advantages such as *sharp* visible emission bandwidth, photo-stability, non-toxicity, higher biocompatibility, which can easily invade the organism for small size particle [18, 19]. Thus, $\text{Er}^{3+}/\text{Yb}^{3+}$ co-doped UCL micro- and nano-scale UC phosphor is regarded as an

ideal choice for detection of temperature in biology.

Double molybdates $\text{NaLn}(\text{MoO}_4)_2$ ($\text{Ln} = \text{RE}^{3+}$) with scheelite-type tetragonal symmetry have excellent physical and thermal stability, and they have proved to be perfect UC phosphor hosts [20]. Recent investigations showed that the *morphologies* of micro- and nano-sized double molybdates based phosphor particles could be controlled by different synthesis methods or parameters [21-23]. In this paper, UC phosphors based on $\text{Yb}^{3+}/\text{Er}^{3+}$ co-doped $\text{NaLa}(\text{MoO}_4)_2$ shuttle-like microcrystal were prepared by hydrothermal process without any surfactants or organic solvents. The uniform and fusiform phosphor particles were obtained through changing the pH value of initial reaction solution and reaction time, and the formation process of shuttle-like microcrystal was proposed according to above results. The UC luminescence, emission mechanisms and temperature-dependent UC spectra were investigated in detail. Their potential application in optical temperature sensor *has* also been evaluated based on the variation of FIR at different temperature.

2. Experimental

2.1. Synthesis of samples

For the synthesis of the $\text{NaLa}(\text{MoO}_4)_2: 0.01\text{Er}^{3+}, 0.10\text{Yb}^{3+}$ micro-architectures, high purity rare earth oxides La_2O_3 , Yb_2O_3 and Er_2O_3 (99.99%), analytical purity sodium hydroxide NaOH and ammonium molybdate tetrahydrate $(\text{NH}_4)_6\text{Mo}_7\text{O}_{24}\cdot 4\text{H}_2\text{O}$ were used as the starting materials without further purification. $\text{La}(\text{NO}_3)_3$, $\text{Yb}(\text{NO}_3)_3$ and $\text{Er}(\text{NO}_3)_3$ solutions were obtained firstly by dissolving La_2O_3 , Yb_2O_3 and Er_2O_3 in nitric acid HNO_3 with constant stirring and heating until all powders completely dissolved. Then the stoichiometric amounts of $(\text{NH}_4)_6\text{Mo}_7\text{O}_{24}\cdot 4\text{H}_2\text{O}$ was added to above solutions with stirring for 30 minutes. Next, the pH values of solution were adjusted to 5, 6, 7, 8 and 9 by adding NaOH solution along with some slurry-like white colloidal precipitates. The mixture was subsequently transferred into a 100 ml Teflon vessel and sealed in a stainless steel autoclave. The autoclave with its contents was treated under hydrothermal conditions for different times at 180 °C. When the reaction completed, it was naturally cooled to room temperature, a white precipitate was obtained. Afterwards, the precipitates were filtered and washed by centrifugation using deionized water and ethanol for several times. The final *products*

were dried at 70 °C for 24 h in air.

2.2 Characterization

The crystal structures were identified by powder X-ray diffractions (XRD) using a Rigaku-Dmax 3C powder diffractometer (Rigaku Corp, Tokyo, Japan) with Cu-K α radiation ($\lambda = 1.5406 \text{ \AA}$). The size and *morphologies* of the as-synthesized sample particles were determined using a Hitachi SU-8010 field emission scanning electron microscope (FE-SEM) operated at an accelerating voltage of 5 kV. Transmission electron microscope (TEM) and high-resolution transmission electron microscopy (HRTEM) were recorded on an FEI TF-20 at an accelerating voltage of 200 kV. UC spectra of samples at room temperature (RT) were recorded using a Hitachi F-4600 spectrophotometer using an external power-controllable 980 nm semiconductor laser as the excitation source. For temperature-dependent UC emission spectra at RT-240 °C, the sample was placed in a temperature-controlled copper cylinder to be characterized using a Jobin-Yvon HRD-1 double monochromator equipped with a Hamamatsu R928 photomultiplier. The excitation power density of the 980 nm laser diode excitation source is about 6W/cm². The signal was analyzed by an EG&G 7265 DSP Lock-in amplifier and stored into computer memories.

3. Results and discussion

3.1 Phase and morphology of NaLa(MoO₄)₂: Er³⁺/ Yb³⁺ microcrystals

The phase *compositions* and crystal *structures* of all samples were characterized by XRD analysis. Figure 1 shows the XRD patterns of NaLa(MoO₄)₂: 0.01Er³⁺, 0.1Yb³⁺ phosphors synthesized at 180 °C for 12 h with different pH values. Results reveal that the pH values of the initial reaction solution play a crucial factor on controlling the formation of phase. Seen from Fig. 1(a), it is clearly found that some diffraction peaks from impurities La₂Mo₃O₁₂ (★), NaMo₃O₁₂ (▼) and La₂MoO₅ (*) as the value of pH = 5 due to the shortage of base NaOH. Here, *the dosage of NaOH was determined by the pH values of reaction solution*. Starting from the value of pH=6, the diffraction peaks of all obtained samples match well with those of standard data of tetragonal structure NaLa(MoO₄)₂ (JCPDS card No. 24-1103) and no any additional diffraction peaks from other impurities can be detected. In addition, the parameters of doped samples were calculated to be about $a=b=5.328 \text{ \AA}$, $c=11.713 \text{ \AA}$ and $V=332.503 \text{ \AA}^3$, which are smaller than those of blank

$\text{NaLa}(\text{MoO}_4)_2$ $a=b=5.343 \text{ \AA}$, $c=11.743 \text{ \AA}$ and $V=335.235 \text{ \AA}^3$ due to the smaller radius of Yb^{3+} (0.985 \AA) and Er^{3+} (1.004 \AA) than that of La^{3+} (1.16 \AA) leading to the shrinking of the lattice constants. Above results suggest that the Er^{3+} or Yb^{3+} ions have effectively incorporated into host lattices by replacing La^{3+} sites without altering the host structure and the well-crystallized $\text{NaLa}(\text{MoO}_4)_2$ samples can be obtained in present hydrothermal conditions.

To further understand the *effects* of pH values on the microstructure and morphology of samples, the SEM of sample $\text{NaLa}(\text{MoO}_4)_2: 0.1\text{Yb}^{3+}, 0.01\text{Er}^{3+}$ particles obtained at controlled experimental condition (180 °C, 12 h) with different pH values are displayed in Fig. 2A-D, respectively. It can be found that the *morphologies* and size of sample particles can be tailored by adjusting the starting pH values of initial reaction solution. The non-uniform and irregular shuttle-like microcrystals were formed as pH= 6, which are shown in Fig. 2A. As the pH value increases to 7, the final *products are* composed of mono-dispersed particles with well-defined shuttle-like morphology (as shown in Fig. 2B), which is more uniform than that of obtained at pH= 6. With further increasing pH values to 8 (Fig. 2C), regular fusiform morphology of particle began to disappear and dissolve into aggregated smaller particles. Finally, the shuttle-like shape particles completely disappeared at pH = 9 (Fig. 2D). According to above results, it can be concluded that the pH values of initial reaction solution dramatically influence the formation and final *morphologies* of products in the hydrothermal process [24], because the pH value of the precursor solution could effectively affect the balance between the rate of ionic migration and the chemical potential in the reaction system, affecting the size and morphology of the final products [25].

3.2 Formation mechanism of shuttle-like $\text{NaLa}(\text{MoO}_4)_2: \text{Er}^{3+}/\text{Yb}^{3+}$ microcrystals

It is found that the *morphologies* and size distribution of sample particles are greatly affected by the reaction time and pH value of precursor solution. Above results indicate that the samples with regular and uniform shape could be obtained at pH= 7. In order to discuss the crystal growth mechanisms, the morphological evolution of shuttle-like $\text{NaLa}(\text{MoO}_4)_2: 0.1\text{Yb}^{3+}, 0.01\text{Er}^{3+}$ was investigated as a function of reaction time at 180 °C and pH= 7. Up to now, the actual crystallization mechanism is no very clear, but the Ostwald ripening process is usually accepted to account for the growth process. Figure 3 shows the FE-SEM of samples obtained after different reaction time, respectively. It is found that irregular and non-uniform crystals were formed and the

most of produce exhibited rough surface after hydrothermal reaction for 1 h (Fig. 3A). More small crystal nuclei attached on the surface of crystals with the reaction time increase up to 6 h (Fig. 3B), which means the crystal growth is along a lattice plane due to their Ostwald's ripening process and higher surface energy drove by the minimization of interfacial energy by reducing the nucleating centers [26]. When the hydrothermal reaction time is 12 h (Fig. 3C), most crystals gradually grew into fusiform structure on the basis of framework at the expense of smaller crystals. As the reaction time was prolonged to 24 h (Fig. 3D), the surfaces of the uniform and well-defined shuttle-like micro-crystals with an average 2 μm length and 1 μm width become smooth. However, the $\text{NaLa}(\text{MoO}_4)_2$ microcrystals become smaller and gradually deviate from fusiform shape with further prolonging the reaction time to 48 h (Fig. 3E). Above results describe the change of an inhomogeneous structure over time and suggest that the formation of $\text{NaLa}(\text{MoO}_4)_2$ micro-crystals may undergo a crystallization, dissolution, re-crystallization and re-dissolution four stage during the whole process. This is a thermodynamics-driven spontaneous process, in which the reduction of surface energy is the main driving forces of particle growth. At the initial stage tiny crystalline nuclei have a larger surface energy and tend form larger crystals, in which small crystals or particles dissolve and re-deposition of the dissolved species on the surfaces of crystals to achieve a stable state and form larger crystal. Due to the different surface energy of each crystal faces, leading to the crystal nucleus to select adsorption on different faces, which would encourage the formation of the final morphology with the minimization of high surface energy faces.

Basing on the above discussion, the morphology evolution process of shuttle-like $\text{NaLa}(\text{MoO}_4)_2: 0.01\text{Er}^{3+}, 0.10\text{Yb}^{3+}$ microstructure could be carefully elucidated as follows. Initially, direct mixing of solutions containing $\text{Ln}(\text{NO}_3)_3$: ($\text{Ln} = \text{La}, \text{Er}, \text{Yb}$) and $(\text{NH}_4)_6\text{Mo}_7\text{O}_{24}$ yielded a supersaturated medium and led to formation of a large number of amorphous particles of sample $\text{NaLa}(\text{MoO}_4)_2: \text{Er}^{3+}/\text{Yb}^{3+}$, which served as precursors of the crystal. The second is hydrothermal reaction process whose main function of hydrothermal process is to crystallize. During this process, the precursors firstly dissolved and tiny particles nucleated, and hydroxy anions were absorbed selectively. Finally, the crystal grew with certain face and shuttle-like crystals appeared. The receivable formation mechanism of $\text{NaLa}(\text{MoO}_4)_2$ monocrystalline is schematically illustrated in Scheme 1. It is well-known that the hydroxyl groups attached in the crystals surface will hinder the UC luminescence. Hence, the samples were calcined at 600 $^\circ\text{C}$ for

1 h to remove the surface functional groups. As shown in Fig. 3F, the product still remained shuttle-like morphology after calcination.

In order to further investigate details the morphological and structural features, the TEM and HRTEM images of sample $\text{NaLa}(\text{MoO}_4)_2: 0.1\text{Yb}^{3+}, 0.01\text{Er}^{3+}$ obtained at $\text{pH}=7$ and 180°C for 24 h were shown in Fig. 4, which *demonstrates* that all of as-synthesized microcrystals are identical shuttle-like morphology and well-separated from each other (as shown in Fig. 4A). A individual and separated $\text{NaLa}(\text{MoO}_4)_2$ particle was also displayed in Fig. 4B, the HRTEM image of its top region was shown in Fig. 4C. The lattice interplanar spacing in the HRTEM image is determined to be 0.494 nm, which correspond to the d spacing for the (101) plane of tetragonal $\text{NaLa}(\text{MoO}_4)_2$. It suggests that the growth direction of crystal is perpendicular to the (101) planes. The corresponding selected area electron diffraction (SAED) pattern in Fig. 4D *indicates* that the single crystalline nature of the shuttle-like $\text{NaLa}(\text{MoO}_4)_2$ particle instead of aggregation of numerous small crystals [27].

3.3 UC properties

Figure 5 shows the UC luminescence spectra at room temperature of phosphors $\text{NaLa}(\text{MoO}_4)_2: 0.1\text{Yb}^{3+}, 0.01\text{Er}^{3+}$ annealed at 600°C for 1 h and un-annealed samples with the excitation of 980 nm laser. It is clearly observed that the UC emission intensity is greatly enhanced after calcinations, and its UC intensity is about 1070 times than that of the sample without sintering due to the disappearance of hydroxy functional groups adhered on the surface of the crystals. As displayed in Fig. 5, the UC spectrum of sample without calcinations is magnified 10^3 times and shown in the inset. Their UC spectra are composed of two green emission bands and a red emission band, which are assigned to ${}^2\text{H}_{11/2} \rightarrow {}^4\text{I}_{15/2}$ (530 nm), ${}^4\text{S}_{3/2} \rightarrow {}^4\text{I}_{15/2}$ (550 nm) and ${}^4\text{F}_{9/2} \rightarrow {}^4\text{I}_{15/2}$ (660 nm) transitions of Er^{3+} , respectively [28].

The UC mechanism is usually determined according to the dependence of UC luminescence intensities on pump power, in which the individual UC emission bands intensity (I) is proportional to the n th power of the pumping laser powder (P), *i. e.*, $I \propto P^n$, where n denotes the number of pumping photons absorbed *per* up-converted photon emitted [29]. In the log-log plots for the integrated UC green (from 500-575 nm) and red emission (from 600 to 675 nm) intensity of phosphor $\text{NaLa}(\text{MoO}_4)_2: 0.1\text{Yb}^{3+}, 0.01\text{Er}^{3+}$ with optimal composition as function of excitation power (Fig. 6A), the slope for the green emission (${}^2\text{H}_{11/2}/{}^4\text{S}_{3/2} \rightarrow {}^4\text{I}_{15/2}$) and red emission

(${}^4F_{9/2} \rightarrow {}^4I_{15/2}$) is 2.16 and 1.98, respectively. This indicates that UC process involves two and three-photon absorption for green emission and two-photon absorption process are involved for red emission at 980 nm, respectively.

The electronic energy levels of Er^{3+} and Yb^{3+} and the possible UC processes in $\text{Yb}^{3+}/\text{Er}^{3+}$ co-doped $\text{NaLa}(\text{MoO}_4)_2$ phosphors were shown Fig. 6B according to the UC mechanisms of the green and red emission. Under 980 nm excitation, the excited state ${}^2F_{5/2}$ energy level of Yb^{3+} is populated through absorbing an infrared photon from its ground state ${}^2F_{7/2}$ (GSA). Also, some Er^{3+} ions can absorb infrared photon to enable the transition from the ground level ${}^4I_{15/2}$ to the excited level ${}^4I_{11/2}$ (ground state absorption, GSA). Due to the energy level difference between ${}^2F_{5/2}$ and ${}^2F_{7/2}$ of Yb^{3+} is close to that of ${}^4I_{11/2}$ and ${}^4I_{15/2}$ from Er^{3+} , the population of ${}^4I_{11/2}$ level could occur through an efficient energy transfer process (ET) from Yb^{3+} to Er^{3+} : $\text{Er}^{3+} ({}^4I_{15/2}) + \text{Yb}^{3+} ({}^2F_{5/2}) \rightarrow \text{Er}^{3+} ({}^4I_{11/2}) + \text{Yb}^{3+} ({}^2F_{7/2})$. For the green emission band peaked at 530 (${}^2H_{11/2} \rightarrow {}^4I_{15/2}$) and 550 (${}^4S_{3/2} \rightarrow {}^4I_{15/2}$) nm, where ${}^2H_{11/2}$ levels were populated through non-radiative (NR) transition from ${}^4F_{7/2}$ of Er^{3+} to ${}^2H_{11/2}$ level, then some of the Er^{3+} in the level ${}^2H_{11/2}$ non-radiatively decay to the ${}^4S_{3/2}$ level. Finally, the levels ${}^2H_{11/2}$ and ${}^4S_{3/2}$ radiatively transit to ground state ${}^4I_{15/2}$ through emitting 530 and 550 nm green lights, respectively. During the process, the population of excited state ${}^4F_{7/2}$ of Er^{3+} involved two and three-photon process according to UC mechanisms, the former two-photon absorption may include three processes:

- (1) $\text{Er}^{3+} ({}^4I_{11/2}) + \text{a photon (980 nm)} \rightarrow \text{Er}^{3+} ({}^4F_{7/2})$ (excited state absorption: ESA),
- (2) $\text{Er}^{3+} ({}^4I_{11/2}) + \text{Yb}^{3+} ({}^2F_{5/2}) \rightarrow \text{Er}^{3+} ({}^4F_{7/2}) + \text{Yb}^{3+} ({}^2F_{7/2})$ (energy transfer: ET),
- (3) $\text{Er}^{3+} ({}^4I_{11/2}) + \text{Er}^{3+} ({}^4I_{11/2}) \rightarrow \text{Er}^{3+} ({}^4F_{7/2}) + \text{Er}^{3+} ({}^4I_{15/2})$ (cross relaxation: CR)

For the three-photon absorption may involve process $\text{Er}^{3+} ({}^4I_{13/2}) + \text{a photon (980 nm)} \rightarrow \text{Er}^{3+} ({}^4F_{9/2})$ (ESA) and $\text{Er}^{3+} ({}^4I_{11/2}) + \text{Yb}^{3+} ({}^2F_{5/2}) \rightarrow \text{Er}^{3+} ({}^4F_{7/2}) + \text{Yb}^{3+} ({}^2F_{7/2})$ (ET), where ${}^4I_{13/2}$ and ${}^4I_{11/2}$ levels are populated by ${}^4I_{11/2} \rightarrow {}^4I_{13/2}$ and ${}^4F_{9/2} \rightarrow {}^4I_{11/2}$ two NR processes. For the red emission, it originates from the ${}^4F_{9/2} \rightarrow {}^4I_{15/2}$ (660 nm) transitions of Er^{3+} , the population of ${}^4F_{9/2}$ can achieve through further NR from ${}^4S_{3/2}$. In addition, the energy ${}^4F_{9/2}$ can also be populated by $\text{Er}^{3+} ({}^4I_{13/2}) + \text{a photon (980 nm)} \rightarrow \text{Er}^{3+} ({}^4F_{9/2})$ (ESA) and $\text{Yb}^{3+} ({}^2F_{5/2}) + \text{Er}^{3+} ({}^4I_{13/2}) \rightarrow \text{Yb}^{3+} ({}^2F_{7/2}) + \text{Er}^{3+} ({}^4F_{9/2})$ (ET) process, in which the ${}^4I_{13/2}$ energy level is populated by NR from ${}^4I_{11/2}$ to ${}^4I_{13/2}$ of Er^{3+} .

3.4 Optical temperature sensing properties

The energy gap ΔE between ${}^2H_{11/2}$ and ${}^4S_{3/2}$ of Er^{3+} is about 780 cm^{-1} and locates in the range of

$200 \text{ cm}^{-1} < \Delta E < 2000 \text{ cm}^{-1}$ [30, 31], which matches well with the requirement to the thermally coupled levels for FIR based optically temperature sensor. The relative population of the two thermally coupled multiplets fits a Boltzmann distribution law and the relative population of the thermally coupled energy levels can be written as follows [32]:

$$\text{FIR} = \frac{I_H}{I_S} = \frac{N(^2H_{11/2})}{N(^4S_{3/2})} = \frac{g_H \sigma_H \omega_H}{g_S \sigma_S \omega_S} \exp\left(\frac{-\Delta E}{KT}\right) = C \exp\left(\frac{-\Delta E}{KT}\right) \quad (1)$$

Where I_H and I_S are intergrated intensities of $^2H_{11/2} \rightarrow ^4I_{15/2}$ (from 510 to 540 nm) and $^4S_{3/2} \rightarrow ^4I_{15/2}$ (from 540 to 570 nm) thermally coupled levels transitions, respectively. N , g , σ , ω are the number of ions, the degeneracy, the emission cross-section, the angular frequency of fluorescence transitions from the $^2H_{11/2}$ and $^4S_{3/2}$ levels to the $^4I_{15/2}$ level, respectively. K is the Boltzmann constant, and ΔE is the energy gap between the $^2H_{11/2}$ and $^4S_{3/2}$ levels, T is absolute temperature and C is the proportionality constant that is defined as: $g_H \sigma_H \omega_H / g_S \sigma_S \omega_S$. In order to investigate the optical temperature sensing property, the temperature-dependent UC green emission spectra ranging from room temperature 300 to 510 K of UC phosphors $\text{NaLa}(\text{MoO}_4)_2: 0.1\text{Yb}^{3+}, 0.01\text{Er}^{3+}$ without and with calcination at 600 °C for 1 h were shown in Fig. 7A and B, respectively. In this process, the excitation source is a 980 nm laser diode with 130 mW, which is low enough to neglect the heating effect from the pumping source. In order to clearly observe the relative change in the spectra, the emission intensity has been normalized at 530 nm emission peak. Seen from Fig. 7, the position of the green emission bands hardly changes with the increase of temperature. Nevertheless, the emission intensity from $^4S_{3/2} \rightarrow ^4I_{15/2}$ transition declines with the increasing of temperature, which means that the fluorescence intensity ratios (FIR) of $I_H (^2H_{11/2} \rightarrow ^4I_{15/2})$ to $I_S (^4S_{3/2} \rightarrow ^4I_{15/2})$ gradually increase with rising temperature.

In order to *intuitively observe* the FIR value with temperature *changes*, the behaviors of FIR (I_H/I_S) for $\text{NaLa}(\text{MoO}_4)_2: 0.1\text{Yb}^{3+}, 0.01\text{Er}^{3+}$ samples before and after sintering as a function of temperature are shown in Fig. 8A and B, in which the fitting curve using Eq. (1) are also included. The left column is the sample without sintering, whereas the right column stand for the sample with calcination at 600 °C for 1 h. Fig. 8A shows a monolog plot of the FIR of green UC emissions for the $^2H_{11/2}, ^4S_{3/2} \rightarrow ^4I_{15/2}$ transitions as a function of inverse absolute temperature in the range of 300 to 510 K. The experimental data were fitted by straight line with slope of about

1005 for the sample without sintering and 1035 for the sample with calcination, respectively. Then the energy gap ΔE could be calculated to about 698 and 719 cm^{-1} , those are very close to the previously reported results in the range of *allowable error* [33]. The *dependences* of FIR on temperature are shown in Fig. 8B, the value of the coefficient C is about 25.07 and 24.78 for non-heated and heated sample according to the linear fit of the experimental data. Sensitivity (S) is a crucial parameter for temperature applications, it is necessary to investigate the variation of sensitivity with temperature. The sensitivity has been calculated using the formula [34]:

$$S = \frac{d(R)}{d(T)} = \frac{g_H \sigma_H \omega_H}{g_S \sigma_S \omega_S} \exp\left(\frac{-\Delta E}{KT}\right) \left(\frac{\Delta E}{KT^2}\right) = R \left(\frac{\Delta E}{KT^2}\right) \quad (2)$$

Fig. 8C presents the S as a function of temperature. The obtained sensitivity of $\text{NaLa}(\text{MoO}_4)_2$: $\text{Er}^{3+}/\text{Yb}^{3+}$ without calcination gradually grows and reaches a maximum about 0.0135K^{-1} at 450 K with the increase of temperature; whereas the maximum sensitivity reaches about 0.0131K^{-1} at 510 K in comparison with the same sample with sintering at $600\text{ }^\circ\text{C}$ for 1 h. The maximum sensitivity for the sample with and without calcinations is close within the margin of error and larger than those of Yb^{3+} - Er^{3+} co-doped UC optically temperature sensor, such as La_2O_3 (0.0091K^{-1}), Gd_2O_3 (0.0084K^{-1}), $\text{Ba}(\text{Zr}_{0.2}\text{Ti}_{0.8})\text{O}_3$ - $(\text{Ba}_{0.7}\text{Ca}_{0.3})\text{TiO}_3$ (0.0068K^{-1}), *etc.* [35-39]. Though the difference between their UC emission intensities are large enough, it can be deduced that the different UC intensity of $\text{NaLa}(\text{MoO}_4)_2$: 0.1Yb^{3+} , 0.01Er^{3+} with same crystal morphology has no obvious effect on sensitivity considering the existence of the error.

4. Conclusions

In summary, the $\text{Er}^{3+}/\text{Yb}^{3+}$ ions co-doped $\text{NaLa}(\text{MoO}_4)_2$ UC monodisperse shuttle-like microcrystal phosphors were prepared by hydrothermal method. The pH values of initial reaction solution and reaction time play crucial role for final perfect morphology, and the optimal reaction condition to obtain regular and uniform shuttle-like particles is $180\text{ }^\circ\text{C}$ for 24 h at pH= 7. The $\text{NaLa}(\text{MoO}_4)_2$: $\text{Er}^{3+}/\text{Yb}^{3+}$ microcrystals emit green light under 980 nm excitation and their UC spectra are composed of prominent green emission centered at 530, 550 nm and red emission peaked at 660 nm originating from $^2\text{H}_{11/2} \rightarrow ^4\text{I}_{15/2}$, $^4\text{S}_{3/2} \rightarrow ^4\text{I}_{15/2}$ and $^4\text{F}_{9/2} \rightarrow ^4\text{I}_{15/2}$ transitions of Er^{3+} ion, respectively. Possible UC processes and mechanism investigation indicate that the green (550

nm) emission may involve two and three-photon process, but red emission (660 nm) is two-photon process. Calcination process did not change the morphology of the sample, but greatly enhance the UC intensity of phosphor. Temperature sensing properties of $\text{NaLa}(\text{MoO}_4)_2: \text{Er}^{3+}/\text{Yb}^{3+}$ shuttle-like microcrystals without and with calcination at 600 °C for 1 h were investigated in the range of 300-510 K. The maximum sensitivity for the sample without sintering reaches 0.0135 K^{-1} at 450 K, whereas the maximum sensitivity reaches 0.0131 K^{-1} at 510 K for sample with sintering at 600 °C for 1 h. This result indicates that the different luminescence intensity for $\text{NaLa}(\text{MoO}_4)_2: \text{Er}^{3+}/\text{Yb}^{3+}$ samples with same crystal morphology and size distribution has no remarkable effect on the value of sensitivity.

Acknowledgments

This work was supported by the high-level talent project of Northwest University, National Natural Science Foundation of China (No. 11274251, 11274299, 11504295), Ph.D. Programs Foundation of Ministry of Education of China (20136101110017), Technology Foundation for Selected Overseas Chinese Scholar, Ministry of Personnel of China (excellent), Natural Science Foundation of Shaanxi Province (No.2014JM1004) and Foundation of Key Laboratory of Photoelectric Technology in Shaanxi Province (12JS094).

References

- [1] X. Liu, C. Yan, J. A. Capobianco, *Chem. Soc. Rev.* 2015, **44**, 1299-1301.
- [2] H. L. Fischer, S. G. Harms, S. O. Wolfbeis, *Chem. Int. Ed. Engl.*, 2011, **50**, 4546–4551.
- [3] V. P. D. Santos, T. M. D. Araujo, S. A. Gouveia-Neto, A. J. Medeiros Neto, B. S. A. Sombra, *Appl. Phys. Lett.*, 1998, **73**, 578–581.
- [4] A. S. Wade, F. S. Collins, W. G. Baxter, *J. Appl. Phys.*, 2003, **94**, 4743–4757.
- [5] B. Hildebrandt, P. Wust, O. Ahlers, A. Dieing, G. Sreenivasa, T. Kerner, H. Riess, *Critical Rev. Oncol./Hematol.*, 2002, **43**, 33–56.
- [6] B. Daniel Jaque, E. M. del Rosal, L. M. Rodríguez, P. H. Maestro, J. G. Solé. *Nanomedicine*, 2014, **9**, 1743-1758
- [7] S. S. Zhou, K. M. Deng, X. T. Wei, G. C. Jiang, C. K. Duan, Y. H. Chen, M. Yin, *Opt. Commun.* 2013, **291**, 138-142.
- [8] C. D. S. Brites, P. P. Lima, N. J. O. Silva, A. Millan, V. S. Amaral, F. Palacio and L. D. Carlos, *New J. Chem.*, 2011, **35**, 1177-1183.
- [9] F. Vetrone, R. Naccache, A. Zamarroón, A. J. Fuente, F. Sanz-Rodríguez, L. M. Maestro, E. M. Rodríguez, D. Jaque, J. G. Sole', J. A. Capobianco, *ACS Nano*, 2010, **4**, 3254-3258.
- [10] Y. J. Ming, H. Yang, L. Lin, Quantum dot nano thermometers reveal heterogeneous local thermogenesis in living cells, *ACS Nano*, 2011, **5**, 5067-5071.
- [11] H. Peng, M. I. J. Sitch, J. Yu, L. N. Sun, L. H. Fischer and O. S. Wolfbeis, *Adv. Mater.*, 2010, **22**, 716-719.
- [12] Binnemans. K, *Chem. Rev.*, 2009, **109**, 4283–4374.
- [13] Z. Boruc, M. Kaczkan, B. Fetlinski, S. Turczynski, M. Malinowski, *Opt. Lett.*, 2012, **37**, 5214-5216.
- [14] C. D. S. Brites, P. P. Lima, N. J. O. Silva, A. Millán, V. S. Amaral, F. Palacio, L. D. Carlos, *Nanoscale*, 2013, **5**, 7572-7580.
- [15] S. F. León-Luis, U. R. Rodríguez-Mendoza, E. Lalla and E. L. Víctor Lavín, *Sens. Actuators B*, 2011, **158**, 208-213.
- [16] H. Zheng, B. Chen, H. Yu , J. Zhang, J. Sun, X. Li, M. Sun, B. Tian, S. Fu, H. Zhong, B. Dong, R. Hua, H. Xi, *J. Colloid. Interf. Sci.*, 2014, **420**, 27-34.

- [17] M. Quintanilla, E. Cantelar, F. Cussó, M. Villegas, A. C. Caballero, *Appl Phys. Express*, 2011, **4**, 022601.
- [18] Wang, F, Han, Y, Lim, C. S, Lu, Y, Wang J, Xu, J, Liu, X, *Nature*, 2010, **463**, 1061–1065.
- [19] M. N. Idris, Z. Li, L. Ye, E. K. W. Sim, R. Mahendran, P. C.. Ho, Y. Zhang, *Biomaterials*, 2009, **30**, 5104–5113.
- [20] T. Li, C. Guo, Y. Wu, L. Li, J. H. Jeong, *J Alloy Compd*, 2012, **504**, 107-112.
- [21] Z. Fu, W. Xia, Q. Li, X. Cui, W, Li, *CrystEngComm*, 2012, **14**, 4618–4624.
- [22] W. Bu, Z. Chen, F. Chen, J. Shi, *J. Phys. Chem. C*, 2009, **113**, 12176–12185.
- [23] L. Xu, X. Yang, Z. Zhai, D. Gu, H. Pang, W. Hou, *CrystEngComm*, 2012, **14**, 7330–7337.
- [24] Q. S. Li, C. H. Feng, Q. Z. Jiao, L. Guo, C. M. Liu, H. B. Xu, *Phys. Status Solidi A*, 2004, **201**, 3055–3059.
- [25] J. T. Han, Y.-H. Huang, X. J. Wu, C. L. Wu, W. Wei, B. Peng, W. Huang, J. B. Goodenough, *Adv. Mater*, 2006, **18**, 2145-2148.
- [26] J. G. Li, X. D. Li, X. D. Sun, T. Ikegami and T. Ishigaki, *Chem. Mater*, 2008, **20**, 2274–2281.
- [27] J. Zhang, F. Huang and Z. Lin, *Nanoscale*, 2010, **2**, 18–34.
- [28] H. Suo, C. Guo, L. Li, *Ceram Int*, 2015, **41**, 7017–7020
- [29] L. Li, C. Guo, H. Jiao, T, Li, Jung-Hyun. Jeong, *J. Rare Earths*, 2013, **31**, 1137-1140.
- [30] L. Li, C. Guo, S. Jiang, D. K. Agrawal, T. Li, *RSC Adv*, 2014, **4**, 6391–6396.
- [31] D. He, C. Guo, S. Jiang, N. Zhang, C. Duan, M. Yin and T. Li, *RSC Adv*, 2015, **5**, 1385-1390.
- [32] M. D. Shinn and W. A. Sibley, M. G. Drexhage, R. N. Brown, *Phys. Rev. B*, 1983, **27**, 6635-6648.
- [33] S. A. Wade, S. F. Collins, G. W. Baxter, *J. Appl. Phys*, 2003, **94**, 4743-4756.
- [34] V. K Rai, A. Pandey, R. Dey, *J. Applied Physics*, 2013, **113**, 083104.
- [35] R. Dey and V. K. Rai, *Dalton Trans*, 2014, **43**, 111–118.
- [36] A. Pandey, S. Som, V. Kumar, V. Kumar, K. Kumar, V. K. Rai, H. C. Swart, *Sens. Actuators B*, 2014, **202**, 1305–1312.
- [37] Q. Zuo, L. Luo, Y. Yao, *J Alloy Compd*, 2015, **632**, 711–716.
- [38] O. A. Savchuk, P. Haro-González, J. J. Carvajal, D. Jaque, J. Massons, M. Aguilóa, *Nanoscale*, 2014, **6**, 9727–9733.
- [39] Y. Tian, B. Tian, C. Cui, P. Huang, L. Wang, B. Chen, *RSC Adv*, 2015, **5**, 14123–14128.

Figure captions

Fig. 1 XRD patterns of the $\text{NaLa}(\text{MoO}_4)_2: 0.01\text{Er}^{3+}, 0.1\text{Yb}^{3+}$ with different pH values of initial reaction solution: (a) pH=5; (b) pH=6; (c) pH=7; (d) pH=8; (e) pH=9. (★: $\text{La}_2\text{Mo}_3\text{O}_{12}$, ▼: $\text{NaMo}_3\text{O}_{12}$, *: La_2MoO_5)

Fig. 2 FE-SEM images of $\text{NaLa}(\text{MoO}_4)_2: 0.1\text{Yb}^{3+}, 0.01\text{Er}^{3+}$ crystallites prepared at 180 °C for 12 h at different pH values: (A) pH =6; (B) pH = 7; (C) pH = 8; (D) pH = 9. Insert in panel B shows high magnification of the same sample.

Fig. 3 FE-SEM images of $\text{NaLa}(\text{MoO}_4)_2: 0.1\text{Yb}^{3+}, 0.01\text{Er}^{3+}$ synthesized at 180 °C and pH = 7 with different hydrothermal reaction time: (A) 1 h; (B) 6 h; (C) 12 h; (D) 24 h; (E) 48 h, and (F) after sintering at 600 °C for 1 h for sample obtained at 180°C, pH=7 for 24 h.

Scheme 1 Formation and evolution schematic diagram of the shuttle-like $\text{NaLa}(\text{MoO}_4)_2: 0.01\text{Er}^{3+}, 0.1\text{Yb}^{3+}$ microcrystals throughout the synthetic process.

Fig. 4 TEM images of $\text{NaLa}_{0.89}(\text{MoO}_4)_2: 0.1\text{Yb}^{3+}, 0.01\text{Er}^{3+}$ prepared at 180 °C, pH = 7 for 24 h: (A) multiple particles; (B) single particles, (C) HRTEM image of the tip in the shown particle of B, (D) the corresponding SAED pattern.

Fig. 5 Up-conversion emission spectra of $\text{NaLa}(\text{MoO}_4)_2: 0.1\text{Yb}^{3+}, 0.01\text{Er}^{3+}$ under the excitation of 980 nm diode laser: (A) without calcinations, (B) after heating at 600 °C for 1 h. Insert illuminates the magnified 10^3 times UC spectra of sample without sintering.

Fig. 6 (A) Log-log plot of the UC luminescence intensity of $\text{NaLa}_{0.89}\text{Er}_{0.01}\text{Yb}_{0.1}(\text{MoO}_4)_2$ as a function of pumping power; (B) Energy level diagram of the $\text{Yb}^{3+}, \text{Er}^{3+}$ ions and the proposed UC mechanisms in $\text{Er}^{3+}/\text{Yb}^{3+}$ co-doped $\text{NaLa}(\text{MoO}_4)_2$ under 980 nm excitation.

Fig. 7 Temperature-dependent green UC luminescence spectra of as-synthesized sample under excitation of 980 nm: (A) without calcinations; (B) after heating at 600 °C for 1 h. (The spectra are normalized at 530 nm).

Fig. 8 Temperature-dependent sensitivities of sample $\text{NaLa}(\text{MoO}_4)_2: \text{Er}^{3+}/\text{Yb}^{3+}$. The left column is the sample without calcination and right column stand for the same sample after heating at 600 °C for 1 h.

Figures

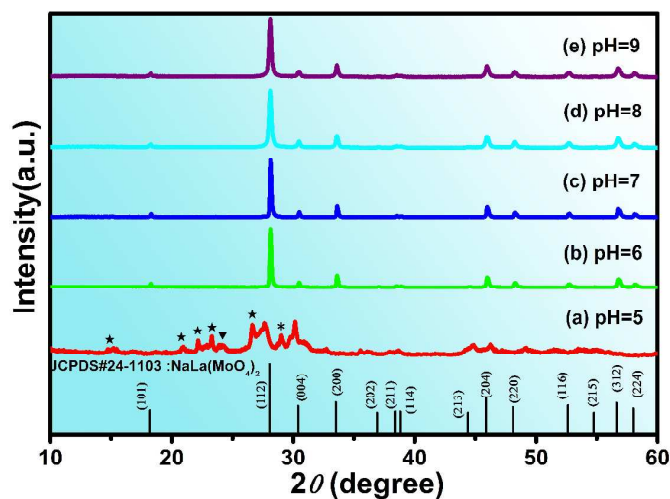


Fig. 1 XRD patterns of the $\text{NaLa}(\text{MoO}_4)_2: 0.01\text{Er}^{3+}, 0.1\text{Yb}^{3+}$ with different pH values of initial reaction solution: (a) pH=5; (b) pH=6; (c) pH=7; (d) pH=8; (e) pH=9. (★: $\text{La}_2\text{Mo}_3\text{O}_{12}$, ▼: $\text{NaMo}_3\text{O}_{12}$, *: La_2MoO_5)

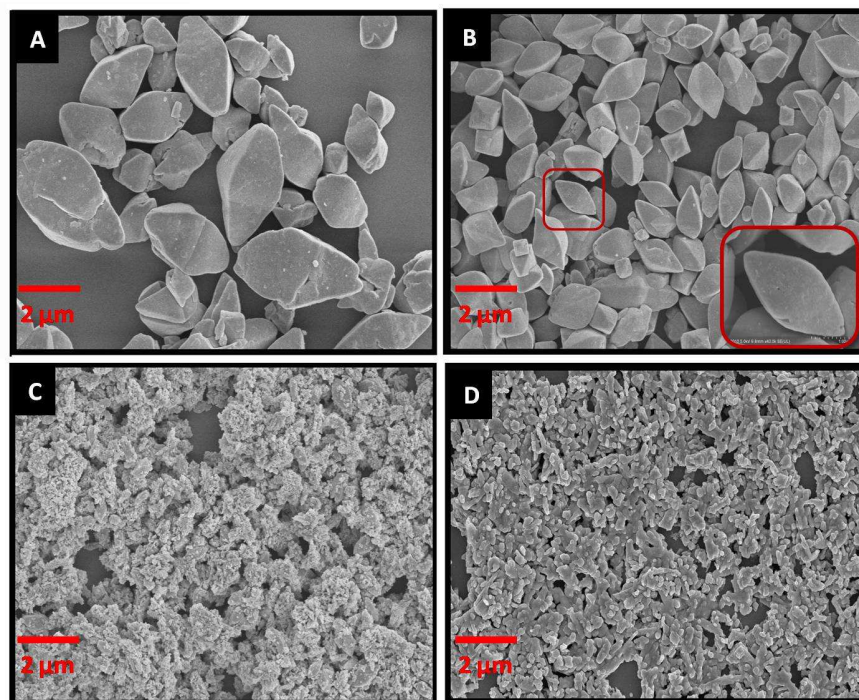


Fig. 2 FE-SEM images of $\text{NaLa}(\text{MoO}_4)_2: 0.1\text{Yb}^{3+}, 0.01\text{Er}^{3+}$ crystallites prepared at $180\text{ }^\circ\text{C}$ for 12 h at different pH values: (A) pH =6; (B) pH = 7; (C) pH = 8; (D) pH = 9. Insert in panel B shows high magnification of the same sample.

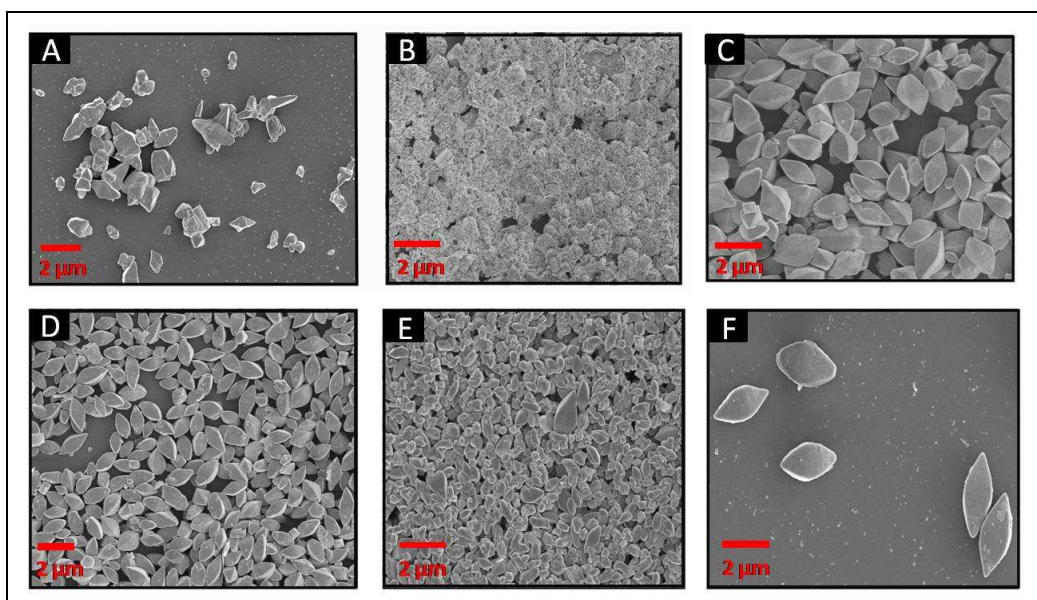
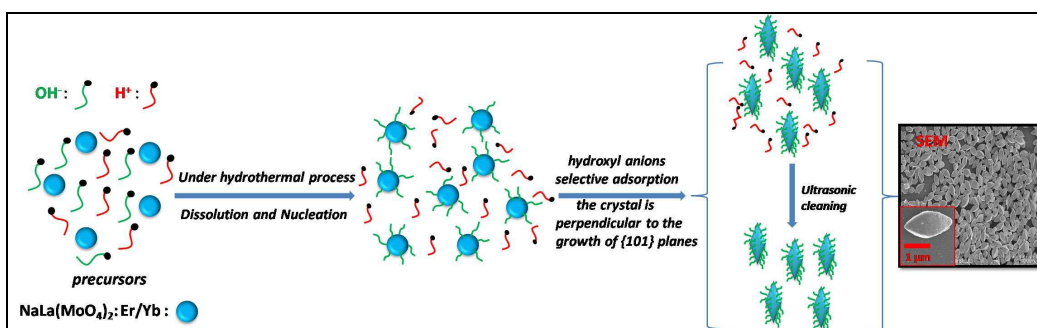


Fig. 3 FE-SEM images of $\text{NaLa}(\text{MoO}_4)_2: 0.1\text{Yb}^{3+}, 0.01\text{Er}^{3+}$ synthesized at $180\text{ }^\circ\text{C}$ and $\text{pH} = 7$ with different hydrothermal reaction time: (A) 1 h; (B) 6 h; (C) 12 h; (D) 24 h; (E) 48 h, and (F) after sintering at $600\text{ }^\circ\text{C}$ for 1 h for sample obtained at $180\text{ }^\circ\text{C}$, $\text{pH}=7$ for 24 h.



Scheme 1 Formation and evolution schematic diagram of the shuttle-like $\text{NaLa}(\text{MoO}_4)_2: 0.01\text{Er}^{3+}, 0.1\text{Yb}^{3+}$ microcrystals throughout the synthetic process.

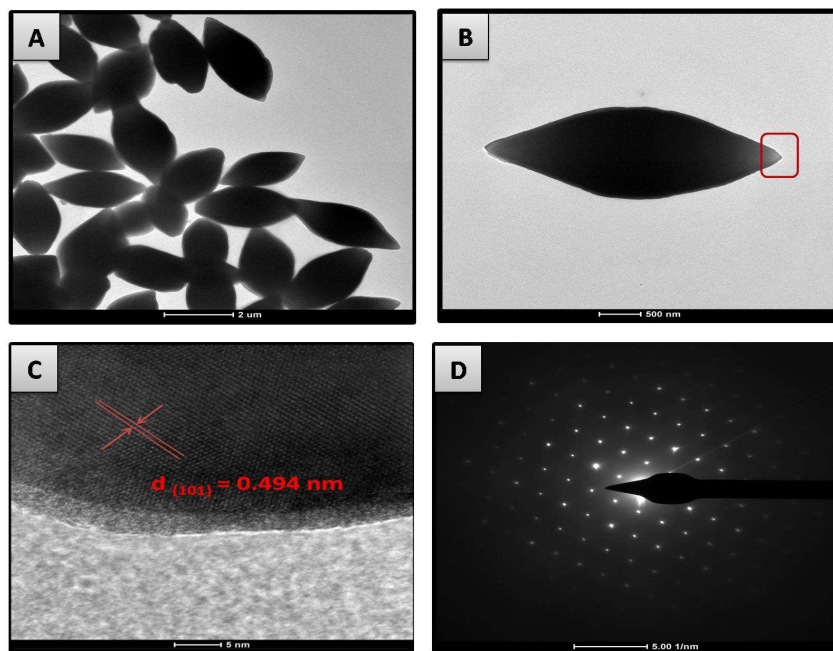


Fig. 4 TEM images of $\text{NaLa}_{0.89}(\text{MoO}_4)_2: 0.1\text{Yb}^{3+}, 0.01\text{Er}^{3+}$ prepared at $180\text{ }^\circ\text{C}$, $\text{pH} = 7$ for 24 h: (A) multiple particles; (B) single particles, (C) HRTEM image of the tip in the shown particle of B, (D) the corresponding SAED pattern.

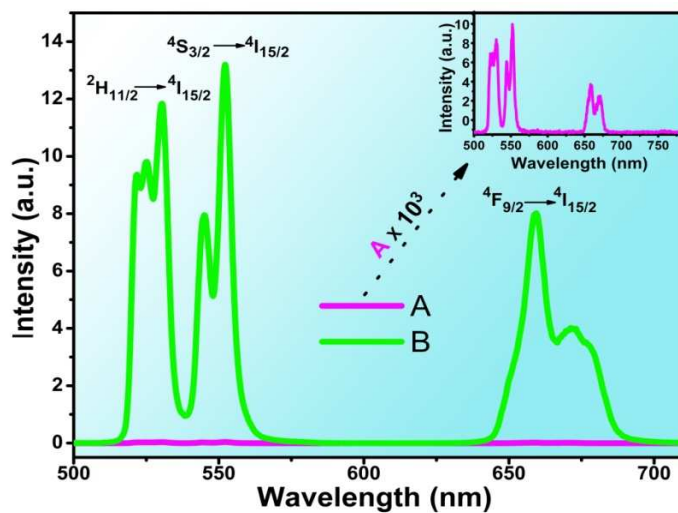


Fig. 5 Up-conversion emission spectra of $\text{NaLa}(\text{MoO}_4)_2: 0.1\text{Yb}^{3+}, 0.01\text{Er}^{3+}$ under the excitation of 980 nm diode laser: (A) without calcinations, (B) after heating at $600\text{ }^\circ\text{C}$ for 1 h. Insert illuminates the magnified 10^3 times UC spectra of sample without sintering.

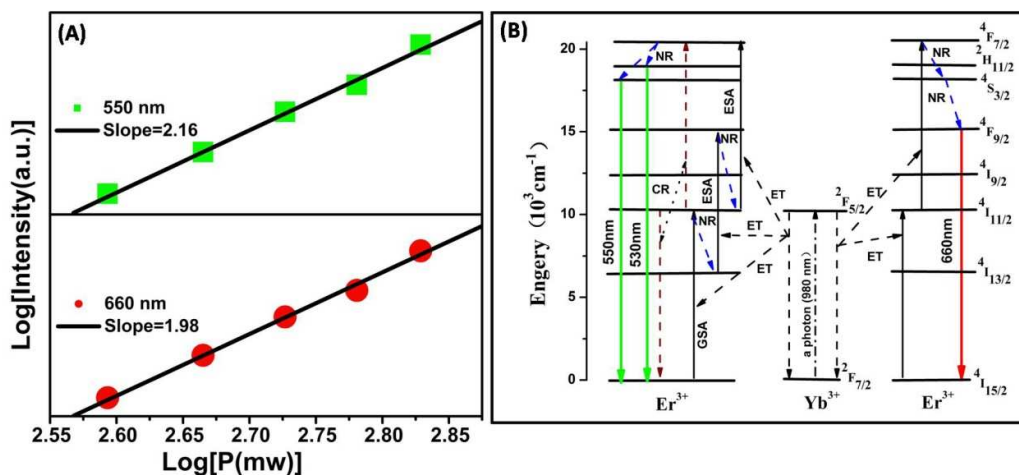


Fig. 6 (A) Log-log plot of the UC luminescence intensity of $\text{NaLa}_{0.89}\text{Er}_{0.01}\text{Yb}_{0.1}(\text{MoO}_4)_2$ as a function of pumping power; (B) Energy level diagram of the Yb^{3+} , Er^{3+} ions and the proposed UC mechanisms in $\text{Er}^{3+}/\text{Yb}^{3+}$ co-doped $\text{NaLa}(\text{MoO}_4)_2$ under 980 nm excitation.

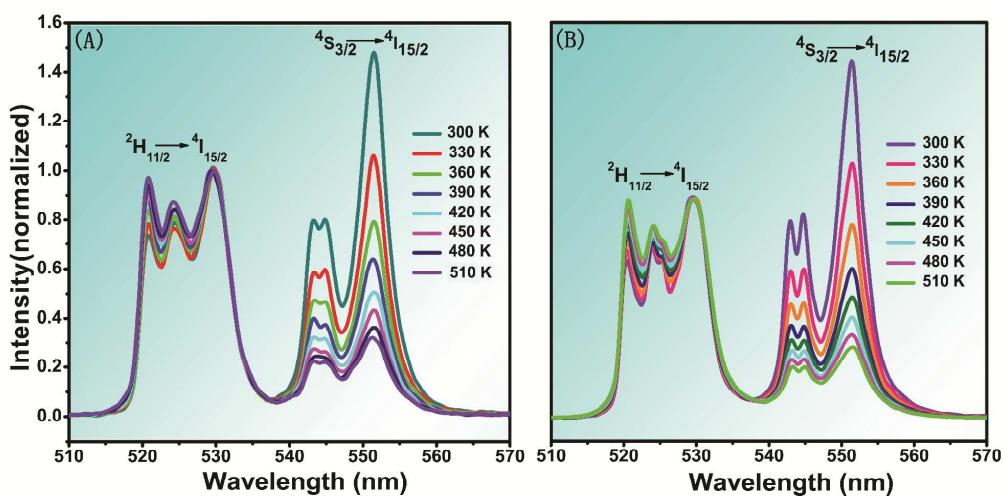


Fig. 7 Temperature-dependent green UC luminescence spectra of as-synthesized sample under excitation of 980 nm: (A) without calcinations; (B) after heating at 600 °C for 1 h. (The spectra are normalized at 530 nm).

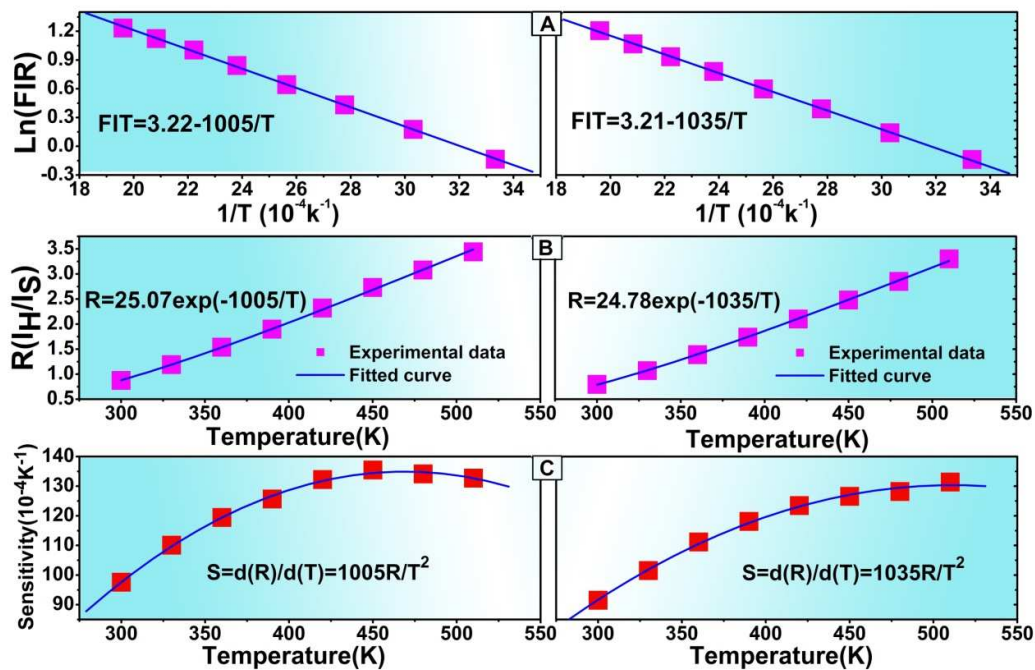
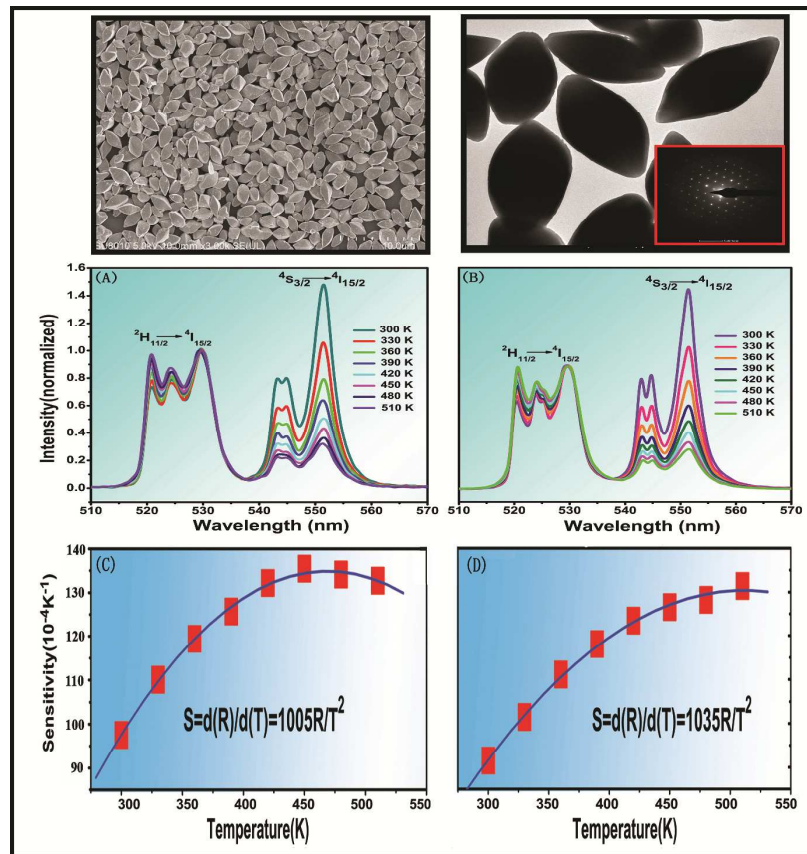


Fig. 8 Temperature-dependent sensitivities of sample $\text{NaLa}(\text{MoO}_4)_2: \text{Er}^{3+}/\text{Yb}^{3+}$. The left column is the sample without calcination and right column stand for the same sample after heating at $600\text{ }^\circ\text{C}$ for 1 h.

Graphic Abstract



SEM of shuttle-like $\text{NaLa}(\text{MoO}_4)_2: \text{Yb}^{3+}, \text{Er}^{3+}$ microcrystals, the temperature-dependent UC spectra and sensitivity of samples without (A, D) and with (B, D) calcinations.